Shear thinning in non-Brownian suspensions explained by variable friction between particles

Laurent Lobry, Elisabeth Lemaire, Frederic Blanc, Stany Gallier, François Peters

Shear thinning in non-Brownian suspensions explained by variable friction between particles

Laurent Lobry[1], Elisabeth Lemaire[1], Frédéric Blanc[1], Stany Gallier[2] and François Peters[1]†

[1]Institut de Physique de Nice, CNRS UCA, Parc Valrose, 06108 Nice cedex 2 France
[2]ArianeGroup, Le Bouchet Research Center, 91710 Vert le Petit, France

(Received xx; revised xx; accepted xx)

We explain shear thinning behavior observed in most concentrated non-Brownian suspensions by variable friction between particles. Considering the low magnitude of the forces experienced by the particles of suspensions under shear flow, it is first argued that rough particles come into solid contact through one or a few asperities. In such a mono-asperity elastic-plastic contact, the friction coefficient is not constant but decreases with normal load. Simulations based on Force Coupling Method are performed either with a constant friction coefficient or a load-dependent friction coefficient. Viscosity measurements are carried out on suspensions of polystyrene particles ($40\mu m$ in diameter) dispersed in a Newtonian silicon oil. The simulations with a load-dependent friction coefficient qualitatively reproduce the observed shear thinning. Furthermore, the comparison between the simulations conducted either with constant friction coefficient or load-dependent friction coefficient provides a model for the shear-thinning viscosity. In this proposed model for the particles with load-dependent friction coefficient, the effective friction coefficient μ^{eff} is specified by the effective normal contact force which is simply proportional to the shear stress. As the shear stress increases, μ^{eff} decreases and the jamming volume fraction increases, leading to the reduction of the viscosity. A very good agreement between the model and the simulations is found and the overall agreement between the model and the experiments is satisfactory, especially regarding the variation of the jamming fraction with the shear stress. The closeness between the experiments and the results of the model enables us to evaluate the friction coefficient for each applied shear stress from the rheometric measurements.

Key words:

1. Introduction

Suspensions of rigid particles in low Reynolds number flows are ubiquitous in industry (food transport, cosmetic products, civil engineering, etc.) or natural flows (such as mud or lava flows) to mention but a few. This wide occurrence of suspensions has fostered significant research in the past years that has revealed a great complexity in the behavior of these systems. Concentrated suspensions may present shear-thinning or shear-thickening behaviors, anisotropic normal stresses, irreversibility under oscillating shear

† Email address for correspondence: francois.peters@unice.fr

and many other complex behaviors. Some of these features come from the possible complexity of the suspensions themselves. For instance, the suspending liquid may be non-Newtonian, particles may have irregular shape, be elongated or faceted, be deformable or polydisperse, they may interact through colloidal forces, Brownian or buoyancy forces may exist... But, it is quite fascinating that even very simple "model" suspensions made of non-Brownian, non-colloidal, monodisperse spherical particles dispersed in a Newtonian fluid exhibit non-Newtonian behaviours. Most of these behaviors may be explained by the coupling between flow, contact interactions and microstructure. To mention just a few examples, Pham *et al.* (2015) showed that irreversible dynamics of non-Brownian neutrally buoyant particles subjected to a periodic shear flow originates in particle solid-solid contacts. Gadala-Maria & Acrivos (1980) proposed to explain the transient response of the viscosity under shear reversal by the presence of an asymmetric shear-induced microstructure that is broken and re-built along the new direction of the flow. Later Blanc *et al.* (2011) showed that the asymmetry of the microstructure comes from solid contact between particles through the asperities they have at their surface. The involvement of contact forces has also made it possible to explain discontinuous shear-thickening often observed in very concentrated suspensions of non-Brownian spheres (Seto *et al.* 2013; Mari *et al.* 2014) by a transition from frictionless to frictional contacts. The effect of solid friction between particles on both normal stress differences and viscosity of concentrated suspensions is also very significant. Numerical simulations of Gallier *et al.* (2014) showed that changing the friction coefficient, μ, from 0 to 0.5 for a 0.45 volume fraction suspension leads to an increase of the viscosity by a factor of 1.5 at while the first normal stress difference magnitude—which is negative—is divided by almost 2 and the second normal stress is two-fold-increased. As the particle volume fraction, ϕ, increases, the contribution of contact forces to the viscosity becomes more and more important compared to the contribution of hydrodynamic forces. For rough frictional particles with $\mu = 0.5$, hydrodynamic and contact contributions are almost the same for $\phi = 0.4$ but, at $\phi = 0.46$, the contact contribution is around twice the hydrodynamic contribution. So one has to keep in mind that solid contacts between particles is a key ingredient to explain non-Brownian suspension rheology.

Among non-Newtonian behaviors that still raise question, shear-thinning occupies a special place because it is quite ubiquitous and can be observed in most experimental results on shear rate-shear stress dependence but is rarely discussed. A first attempt to explain shear-thinning has been proposed by Acrivos *et al.* (1994) who showed that the apparent shear-thinning that they observed when the viscosity of a suspension of non-Brownian particles is measured in a Couette device is due to a mismatch in the densities of the liquid and of the particles. But whereas this explanation seems compelling in the case of the Couette flow where the larger and larger resuspension of the denser particles as the shear rate increases should lead to a decrease of the measured apparent viscosity, it cannot explain shear-tinning observed in other flow geometries such as for example in torsional parallel-plate flow. Shear-thinning, however, has been reported in rotating parallel plate measurements by several authors (Dbouk 2011; Zarraga *et al.* 2000; Vázquez-Quesada *et al.* 2016). Vázquez-Quesada *et al.* (2016) explains the shear-thinning they observed by the shear-thinning behavior of the suspending liquid (silicon oil) itself. More precisely, the suspending liquid is Newtonian at the macroscopic shear rates involved in the measurement of the viscosity but may be shear-thinning in the range of the higher shear rates experienced by the host liquid in the interparticle gap. Later, the authors showed that this mechanism cannot apply for all systems and suggested that variable contact friction between particles may also be responsible for shear-thinning (Vazquez-Quesada *et al.* 2017).

We explore this idea in the present paper. Prior to describe the contact law between particles, we would like to highlight that particle contacts are enabled by the asperities that are present at particle surface. For perfectly smooth particles, solid contact is prevented by lubrication forces that diverge as the particle separation tends to zero. On the opposite, for rough particles, contact between particles is made possible through isolated asperities that maintain finite lubrication forces between particles. In other words, roughness is able to screen lubrication divergence. In such a scenario, only one or a few asperities may be involved in contact, and the macroscopic Amontons-Coulomb law that is used to describe contact between macroscopic surfaces and according to which the friction coefficient does not depend on the magnitude of the tangential or normal load is expected not to hold anymore. Indeed, this macroscopic contact law is usually understood in the frame of theories where a large number of asperities are compressed (Greenwood & Williamson 1966). Instead, in the case of a small number of elastically contacting asperities, the friction coefficient is expected to decrease with load (Archard 1957).

In the present paper, we modify the contact model presented in (Gallier *et al.* 2014) in order to account for a variable friction between particles. The first part is dedicated to the presentation of the numerical method and of the contact model that has been chosen to introduce a load-dependent friction coefficient in the numerical simulations. The second section presents the simulation results and proposes a model that makes it possible to estimate the influence of any particular friction law on the viscosity without performing new simulations. In the third section, experiments carried out on suspensions of monodisperse polystyrene particles, $40\mu m$ in diameter, dispersed in a silicone oil for five values of the particle volume fraction are presented. And the last section is devoted to a comparison of the numerical model to the experimental results.

2. Numerical method

2.1. *The Force Coupling Method*

We use the Force Coupling Method to study the rheology of non-Brownian suspensions made of rigid particles in a Newtonian liquid, η_0 in viscosity. The main features of the method are recalled in (Peters *et al.* 2016) and the interested reader will find more detail in (Yeo & Maxey 2010). In this method, the motion of the fluid is computed in the whole meshed domain, where the presence of the particles is taken into account using a specified force density that enforces rigid body motion in the particles. Small scale flows between the particles are not resolved by the direct computation, so that the hydrodynamic force and other moments are corrected using theoretical expressions from lubrication approximation. Thus, this method is able to catch both long range and short range hydrodynamic interactions. Inertia is neglected in computing both the liquid and the particle motion, and the particle density is matched to that of the liquid. As a consequence, the total force and torque on each particle vanish.

$$\boldsymbol{F}^h + \boldsymbol{F}^c = 0 \tag{2.1}$$

$$\boldsymbol{T}^h + \boldsymbol{T}^c = 0 \tag{2.2}$$

where the superscript h stands for the hydrodynamic moments (both direct computation and lubrication corrections) and c for the contact moments. The later will be described in the following section, and the former are computed as explained in (Peters *et al.* 2016). The hydrodynamic force moment (stresslet) $\boldsymbol{S^h}$ as well as the contact force moment $\boldsymbol{S^c}$

of each particle are computed too, yielding the effective stress, and then the relative viscosity η^S defined as the ratio of the suspension viscosity to the host liquid viscosity.

The particles are contained in a cubic domain, where the shear rate $\dot{\gamma}$ is imposed. The flow is made periodic in all three dimensions using Lee Edwards conditions. The total solid volume fraction is denoted by ϕ. We consider a bidisperse collection of spheres, of radius a_1 and a_2=1.4 a_1, with the same volume fraction $\phi/2$, in order to avoid crystallisation. The particular value $a_1/a_2 = 1.4$ that was chosen is widely used in the literature (Seto *et al.* 2013; Mari *et al.* 2014; Ness & Sun 2015; Seto *et al.* 2017). We note here that a recent study was published, that explored the influence of bidispersity on the suspension rheology, and compared it to polydisperse system rheology (Pednekar *et al.* 2018). From this study, it is possible to infer that, at least for the volume fraction range that is probed in the present article, the viscosity is nearly the same as for a monodisperse system without crystallisation. The size of the computation cell is $L_x \times L_y \times L_z = 16a_1 \times 16a_1 \times 16a_1$ corresponding to approximately 300 particles for a solid volume fraction ϕ=0.5. The suspension is sheared during a total strain ranging between 40 and 100, depending on the solid volume fraction, in order to obtain correct averaging.

2.2. *Contact model*

2.2.1. *Introduction*

Up to now, most simulations of sheared frictional suspensions (Mari *et al.* 2014; Seto *et al.* 2013; Gallier *et al.* 2014; Peters *et al.* 2016) have considered a simple model of frictional contact with a constant static friction coefficient, as defined by the ratio of the largest tangential force that is allowed before sliding motion occurs to the normal force. In such a model, the friction coefficient is constant whatever the normal force or contact history. In addition, the dynamic friction coefficient, that is observed during sliding motion, and the static friction coefficient are assumed to be equal. It should be noted first that even for contact between macroscopic surfaces, the encountered phenomena are far richer than what is suggested by this very simple Amontons-Coulomb law. The static friction coefficient is usually different from the dynamic friction coefficient that is observed during sliding motion. Both depend on the loading time, and the latter on the sliding velocity. The friction coefficient has also been shown to depend on the applied load (McFarlane & Tabor 1950; Benabdallah & Yelle 1991; Myshkin *et al.* 2006). From a fundamental point of view, it is well understood that the real area of contact is far smaller than the macroscopic contact area, meaning that contact occurs between surface asperities (Tabor 1981). Thus, a deeper understanding of friction between surfaces is to be sought first in the description of single asperity contact, and then in the distribution of contacting asperities. Most of the many models from the litterature concentrate on those aspects. In the modelling of macroscopic contact between macroscopic surfaces, it is usually assumed that a statistically large number of asperities are deformed as in (Greenwood & Williamson 1966). In this particular model, the asperities are supposed to be elastically deformed. Even though the contact area for each single asperity is not proportional to the corresponding load, the total area is approximately proportional to the total load, leading to a static friction coefficient that does not depend on the load, in agreement with Amontons-Coulomb law. Concerning the contact between a single asperity and a smooth surface, many models have been proposed, where the deformation remains elastic at low applied load, and enters a plastic regime as the load is increased (see for example (Chang *et al.* 1987; Brizmer *et al.* 2006*b*, 2007)), and some experimental validations have been performed for the contact of a smooth sphere against a flat substrate, leading to a load-dependent static friction coefficient (Ovcharenko *et al.*

2008). The influence of adhesion on the single asperity contact area has also been studied (Johnson *et al.* 1971; Derjaguin *et al.* 1975).

In the particular field of contacting microparticles, experimental studies have been performed during the last 2-3 decades, by means of the so-called colloidal probe technique, where a single bead, a few microns in diameter typically, is attached to the cantilever of an atomic force microscope (AFM) (see for example the review by Butt *et al.* (2005)). Some of these studies deal with the adhesion and/or friction coefficient between a particle and a hard flat substrate. When experiments are performed in dry atmosphere, a significant adhesion is measured (Schaefer *et al.* 1995; Biggs & Spinks 1998), that may depend on the applied load (Biggs & Spinks 1998) possibly due to plastic deformation of the surface asperities (Reitsma *et al.* 2000). The static friction coefficient is affected by the adhesion forces, so that a finite friction force is observed with vanishing normal load (Biggs & Spinks 1998; Reitsma *et al.* 2000; Ecke & Butt 2001). Adhesion forces between particles have been also measured for smooth particles in air, again leading to a friction coefficient that decreases as the load increases. The intensity of the adhesion depends on the nature of the particles and on the surface roughness (Heim *et al.* 2002; Ling *et al.* 2007). When particles are immersed in water, the interaction forces are more complicated due to electric double layer (Ducker *et al.* 1992; Li *et al.* 1993; Zou *et al.* 2015). In the case of weak adhesion, the friction force between silica particles in a salty alkaline solution has been shown to follow Amontons-Coulomb law (Fernandez *et al.* 2015). This contrasts with the results of the article of Chatté *et al.* (2018) who measured the friction force between PVC particles immersed in an organic Newtonian liquid (Dinch). No adhesion was noticed and the measured friction coefficient decreased with the applied load, due to compressed polymer brushes at the particle surface. To conclude this overview of experimental studies, the friction law between microparticles in a liquid strongly depends on the particular system that is considered, and is affected by adhesion, roughness, plastic deformation and surface coating that may introduce discrepancies with the Amontons-Coulomb law and yield an apparent friction coefficient that decreases as the load increases.

The present paper deals with contacting micro-particles immersed in a host liquid, the whole suspension experiencing a shear flow. This particular problem may be considered quite specific for several reasons. First, the contact forces that are controlled by the sheared suspension bulk stress may be very weak, depending on the shear rate and the volume fraction. As a consequence (Sec. 2.2.3), the elastic contact radius computed for two smooth particle may be smaller than the surface roughness size. This particular point suggests that contact occurs between a small number of asperities. In addition, as explained before and in more detail in Sec. 2.2.3, such a mono-asperity contact is expected to undergo a transition from elastic to plastic deformation. For that reason, we select in this article a particular friction law from the literature, where the decrease of the friction coefficient originates in the non-linear variation of the contact area with the applied load (Brizmer *et al.* 2007) with no adhesion. As previously mentioned, this model properly describes the dry contact between a spherical mono-asperity and a flat surface (Ovcharenko *et al.* 2008). Obviously, this model cannot pretend to full generality. However, as shown in Sec. 2.2.3, it is well supported by qualitative estimation from physical properties of typical suspension components. In addition, as shown in section 3.3, a simple model that allows to compute the suspension viscosity from the microscopic friction law is validated using the simulation output, making it easy to get the suspension viscosity for other types of friction law without performing new simulations.

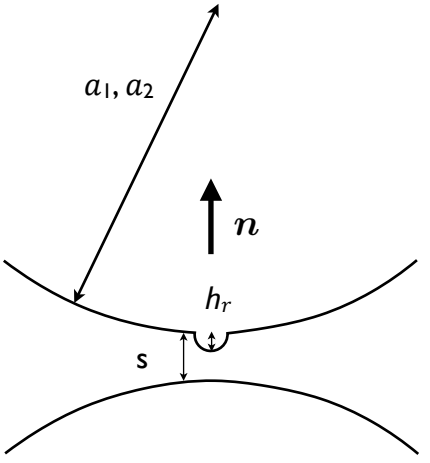

FIGURE 1. Sketch of the roughness modelling. s is the hydrodynamic separation distance, h_r is the roughness height

2.2.2. *An elastic-plastic mono-asperity contact model*

As mentioned above, we consider rough spherical particles of radius a_1 or a_2 that come into contact, through their surface asperities. It is assumed that the whole contact between particles occurs between one single asperity, modeled by a spherical surface with radius h_r, and a smooth patch of the second particle (figure 1). The contact model is adapted from the numerical study by Brizmer *et al.* (2007) where the contact between a sphere (corresponding the asperity in the present article) and a rigid flat under full stick conditions was simulated using the finite element method. The sphere was made of an elastic linear isotropic hardening material, where the Hooke's and Prandtl-Reuss constitutive law governed the elastic and plastic regime, respectively. A normal preload P was applied first and kept constant as the tangential load Q was increased until sliding inception, which was treated as a plastic yield failure. The friction coefficient was defined as the ratio of the largest value of the tangential load Q_{max} to the normal preload P, and a correlation law was fitted to the variation of Q_{max} with P. Two different regimes were identified: when the preload is smaller than a critical value, L_c (equation 2.4), the deformation of the sphere keeps fully elastic during normal loading, and the friction coefficient decreases with the applied preload as $(P/L_c)^{1/3}$. As P is increased, the fraction of the material that experiences plastic deformation increases, and the friction coefficient gradually tends to a constant value. The correlation between the preload P and the surface overlap is also provided, that includes the transition form elastic to plastic regime.

In the present article, the contact force exerted on the smooth patch (figure 1) is split into the force normal to the surfaces, $\boldsymbol{F_n}$ and the tangential force, $\boldsymbol{F_t}$. For the sake of simplicity, the normal force is treated as fully elastic i.e. reversible, although it depends on the surface overlap $\delta = h_r - s$ according to the correlation found by Brizmer *et al.* (2006*a*,*b*). It means that the influence of the hysteresis of the contact law, which is connected to material plasticity, is neglected here. The normal force $\boldsymbol{F_n}$ is given in the elastic regime ($\delta \leqslant \delta_c$, $L \leqslant L_c$) by equation 2.3:

$$\boldsymbol{F_n} = -L_c \left(\frac{\delta}{\delta_c}\right)^{3/2} \boldsymbol{n} \tag{2.3}$$

where L_c and δ_c are the critical normal load and surface overlap at yield inception, respectively:

$$L_c = \bar{L}_c \pi^3 \frac{Y_0}{6} C_\nu^3 \left(h_r \frac{2(1-\nu^2)\ Y_0}{E} \right)^2 \tag{2.4}$$

$$\delta_c = \bar{\delta}_c\ h_r \left[\pi C_\nu\ \frac{(1-\nu^2)\ Y_0}{E} \right]^2 \tag{2.5}$$

E, ν and Y_0 are the Young's modulus , Poisson's ratio and yield strength of the material respectively, and $C_\nu = 1.234 + 1.256\ \nu$. Equations 2.3, 2.4 and 2.5 differ from the usual Hertz contact law between a sphere and a plane half-space made of the same material by the overbar quantities 2.6 and 2.7, that are characteristic of the full stick contact condition:

$$\bar{L}_c = \left[8.88\nu - 10.13\left(\nu^2 + 0.089\right) \right] \tag{2.6}$$

$$\bar{\delta}_c = \left[6.82\nu - 7.83\left(\nu^2 + 0.0586\right) \right] \tag{2.7}$$

In the plastic regime ($\delta > \delta_c$, $L > L_c$), the normal force is softer (Eq. 2.8):

$$\boldsymbol{F_n} = -L_c \left(\frac{\delta}{\delta_c} \right)^{3/2} \left[1 - \exp\left(\frac{1}{1 - \left(\frac{\delta}{\delta_c} \right)^\beta} \right) \right] \boldsymbol{n} \tag{2.8}$$

where β=0.174+0.08 ν. In addition, due to the softness of the normal force, and the high level of contact forces at large shear rate and high solid volume fraction, particles may overlap, meaning that the asperity is fully flattened out, and the distance s may become negative. To avoid this, a multiplying function is included, that goes to infinity for s= 0.2 h_r (δ= 0.8 h_r), so that the distance between particle surfaces, s, is kept larger than 0.2 h_r. This particular value was chosen arbitrarily but has only a quite weak influence on the lubrication stress. Figure 2 displays the interparticular force normalized by critical force L_c as a function of the the dimensionless overlap, δ/h_r . The dashed line is the dimensionless force from equation 2.8, while the solid line displays the force used in the simulations, in order to keep δ/h_r <0.8 as mentioned above. Its expression differs from the original one only for $\delta/h_r \gtrsim 0.7$.

The tangential force is modeled as a linear spring-like force with a threshold as in (Cundall & Strack 1979; Gallier *et al.* 2014; Peters *et al.* 2016):

$$\mathbf{F}_t = \begin{cases} -\kappa_t \mathcal{Y} & \text{for} \quad |\boldsymbol{F_t}| < \mu |\boldsymbol{F_n}| \text{ (stick-phase)} \\ \mu |\boldsymbol{F_n}| \frac{\mathbf{F}_t}{|\boldsymbol{F_t}|} & \text{otherwise (slip-phase)} \end{cases} \tag{2.9}$$

where μ is the (static and dynamic) friction coefficient. $\mathcal{Y}$ is the relative tangential displacement of the two particle surfaces and it is calculated as the integral of the slip velocity during contact (Peters *et al.* 2016). The value of the stiffness of the tangential spring, κ_t, is linked to the normal force intensity $|\boldsymbol{F_n}|$ through equation 2.10 so that it depends on the surface overlap δ (Eq. 2.8).

$$\kappa_t = \frac{2}{7} \frac{|\boldsymbol{F_n}|}{\delta} \tag{2.10}$$

The friction coefficient has been computed by Brizmer *et al.* (2007) as :

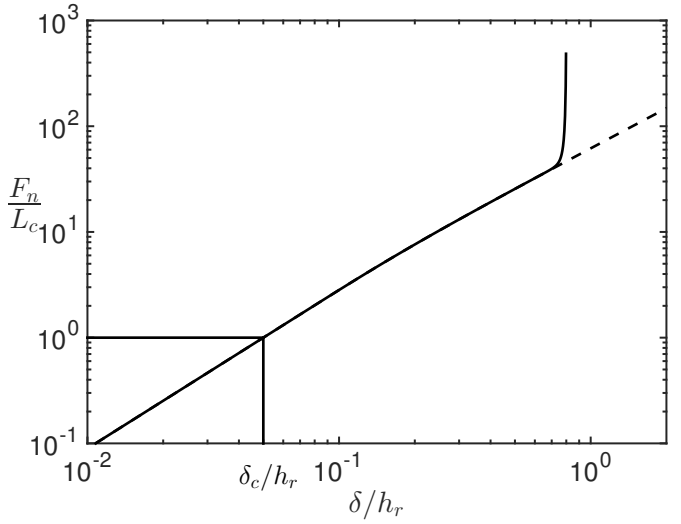

FIGURE 2. Dimensionless normal contact force as a function of dimensionless overlap. Dashed line : original force from equation 2.8. Solid line : corrected force to keep δ/h_r <0.8.

$$\mu = 0.27 coth \left[0.27 \left(\frac{|\boldsymbol{F_n}|}{L_c} \right)^{0.35} \right] \tag{2.11}$$

The last equations deserve a few comments. Firstly, the tangential force in the stick-phase as defined in equations 2.9 and 2.10 is an approximate version of the original model by Brizmer *et al.* (2007). In the present paper, the tangential force (equation 2.9) is assumed to be linear with the tangential displacement, while in the original work of Brizmer *et al.* (2007), the material undergoes plastic deformation, and the force does not depend on the tangential displacement in a strict linear way. In addition, the coefficient 2/7 is smaller than the value $3(1-\nu)/(2-\nu)$ that may be estimated from (Brizmer *et al.* 2007). It is chosen here mostly to be consistent with earlier work (Gallier *et al.* 2014; Peters *et al.* 2016). This particular value was originally chosen to fit experimental data from impact experiments (Shäfer *et al.* 1996). We also stress that the primary aim of the present article is to study the influence of a variable friction coefficient on suspension viscosity.

The most important feature of the model, at least for the present work, is displayed in equation 2.11, i.e. the friction coefficient decreases as the normal force increases. The variation of μ is plotted in figure 3. In the elastic regime ($F_n/L_c < 1$), equation 2.11 yields $\mu \propto (L_c/F_n)^{0.35}$ in approximate agreement with Hertz theory according to which the contact area is proportional to the normal force $A \propto F_n^{2/3}$. Indeed, since sliding inception is modeled as a plastic yield failure, it occurs as the tangential force exceeds $F_t^{max} \propto Y_0 A \propto Y_0 F_n^{2/3}$, leading to $\mu = F_t^{max}/F_n \propto F_n^{-1/3} \sim F_n^{-0.35}$. As the dimensionless normal force F_n/L_c increases far beyond 1, the material in the whole contact zone undergoes plastic deformation, and the contact area is proportional to the normal force, giving the constant friction coefficient μ=0.27. This particular value depends weakly on the material properties (Brizmer *et al.* 2007).

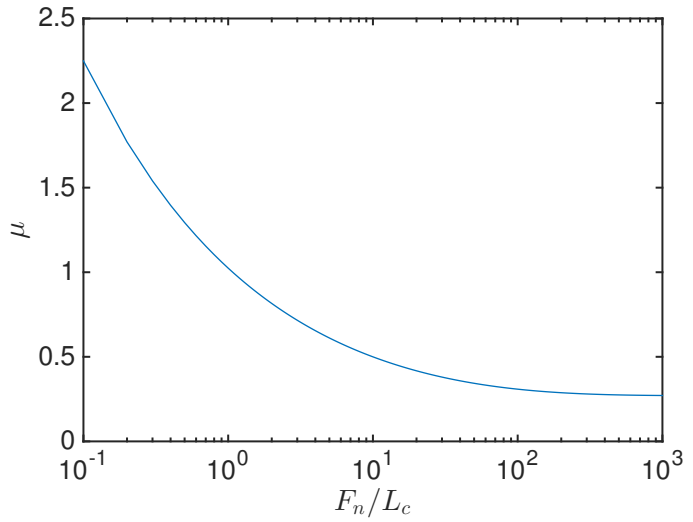

FIGURE 3. Friction coefficient as a function of dimensionless contact normal force (Eq. 2.11)

Young's Modulus	Yield strength	Poisson's ratio	Roughness ratio	Part. radius	Shear rate	Critical load	Length ratio	Reduced shear rate
E (Pa)	Y_0 (Pa)	ν	h_r/a_1	a_1 (μm)	$\dot{\gamma}$ (s^{-1})	L_c (nN)	δ_c/h_r	$\dot{\Gamma}$
$3\ 10^9$	$60\ 10^6$	0.4	$5\ 10^{-3}$	20	$[10^{-2} - 10^2]$	~ 20	$\sim 10^{-2}$	$[4\ 10^{-3} - 4\ 10^1]$

TABLE 1. Typical values of physical parameters

2.2.3. *Dimensionless parameters*

From the microscopic model presented in the last sections, several dimensionless parameters can be indentified from the relevant length scales a_1, a_2, h_r, δ_c, and force scales L_c, $6\pi\eta_0 a_1^2\dot{\gamma}$. The latter is approximately the largest interparticle force experienced by two contacting particles of radius a_1 in a sheared dilute suspension. The value that we chose for the ratio of the roughness height to the smallest radius h_r/a_1=5.10^{-3} is typical for polymer spheres model suspensions (Blanc *et al.* 2011; Moon *et al.* 2015). The interparticle force is completely specified by the critical force L_c and the critical overlap δ_c, so that the relevant dimensionless parameters are the dimensionless shear rate defined as:

$$\dot{\Gamma} = \frac{6\pi\eta_0 a_1^2\dot{\gamma}}{L_c} \tag{2.12}$$

and the ratio of the critical overlap to the roughness height δ_c/h_r.

In addition, in dilute suspensions, the interparticle force level is $F_n \sim 6\pi\eta_0 a_1^2\dot{\gamma}$, so that the value of the reduced shear rate $\dot{\Gamma}$ determines the typical overlap (figure 2) and the typical friction coefficient μ (figure 3). When $\dot{\Gamma} \ll 1$, the contact is mainly elastic ($\delta < \delta_c$) and the typical friction coefficient decreases with shear-rate, while the contact is mainly plastic and the typical friction coefficient tends to a plateau as $\dot{\Gamma} \gg 1$ ($\delta \gg \delta_c$).

Table 1 gathers numerical values for different parameters computed for polystyrene for

	a_2/a_1	h_r/a_1	δ_c/h_r	$\dot{\Gamma}$	ϕ	μ
Load-dependent μ	1.4	$5\ 10^{-3}$	$5\ 10^{-2}$	$[3\ 10^{-3} - 3\ 10^{2}]$	[0.4 ; 0.45 ; 0.47 ; 0.5]	
Constant μ	1.4	$5\ 10^{-3}$	$5\ 10^{-2}$	1	[0.3 ; 0.4 ; 0.45 ; 0.47 ; 0.5]	[0 ; 0.27 ; 0.5 ; 1 ; 2 ; 5 ; 10]

TABLE 2. Simulation parameters

usual values of the shear rate $\dot{\gamma}$. Most importantly, the reduced shear rate $\dot{\Gamma}$ ranges from $4\ 10^{-3}$ to $4\ 10^{1}$, meaning that the contacting material behavior is expected to switch from elastic to plastic as the shear rate is increased. In addition, the initially decreasing friction coefficient will level off at high shear rate.

The small value of the ratio δ_c/h_r indicates that the roughness deformation at yield inception is very low, and supports the idea of a mono-asperity contact, at least for $\dot{\Gamma} \lesssim 1$. In particular, δ_c/h_r turns out to be ratio of the contacting area of the asperity at yield inception, that reads $\pi h_r \delta_c$ for a Hertzian contact, to the asperity effective surface πh_r^2. It is also possible to compute from the usual Hertz scaling the typical radius a_H^{sm} of the contact area between two smooth spheres, a_1 in radius, as the critical load L_c is applied: $a_H^{sm}/h_r = \sqrt{\delta_c/h_r}\,(a_1/2h_r)^{1/3} \sim 0.5$ suggesting again a small number of compressed asperities.

2.3. *Simulation parameters*

From a practical point of view, the variety of the length scales $[\delta_c\ ;\ h_r\ ;\ a_1]$ is quite difficult to deal with in computations, since very small time steps are required to accurately compute the contact dynamics, and quite long deformation is needed for correct averaging. To keep the time step reasonably large (i.e. larger than 10^{-6} in strain units), we set the critical length ratio δ_c/h_r=$5\ 10^{-2}$.

Finally, table 2 gathers the simulation parameters. Besides suspensions of particles displaying load-dependent friction coefficient, suspensions made of particles with constant friction coefficient have been considered as well in a second set of simulations for comparison. The microscopic model is strictly the same, except for equation 2.11.

3. Simulation results

3.1. *Load-dependent friction coefficient*

Figure 4 displays the computed relative viscosity as a function of the reduced shear rate $\dot{\Gamma}$. As expected, as the reduced shear rate increases, the viscosity decreases, due to friction coefficient reduction. The viscosity exhibits two plateaus, one at low reduced shear rate and the other at high reduced shear rate. The latter is due to the saturation of the friction coefficient as F_n/L_c increases. The low shear plateau originates in the saturation of the viscosity as the friction coefficient increases. More quantitatively, as recently shown for monodisperse suspensions (Peters *et al.* 2016) and in more detail in the following, the friction coefficient has a strong influence on the viscosity only in a range of roughly $[0\ ;\ 1-2]$. In the present model, the friction coefficient may vary in the range $[\ 0.27; \infty\ [$ depending on the normal force between particles. For moderately concentrated suspensions, it is thus expected from figure 3 that the viscosity mostly varies when the reduced shear rate $\dot{\Gamma}$ (Eq. 2.12) ranges from 10^{-1} to 10. This is approximately

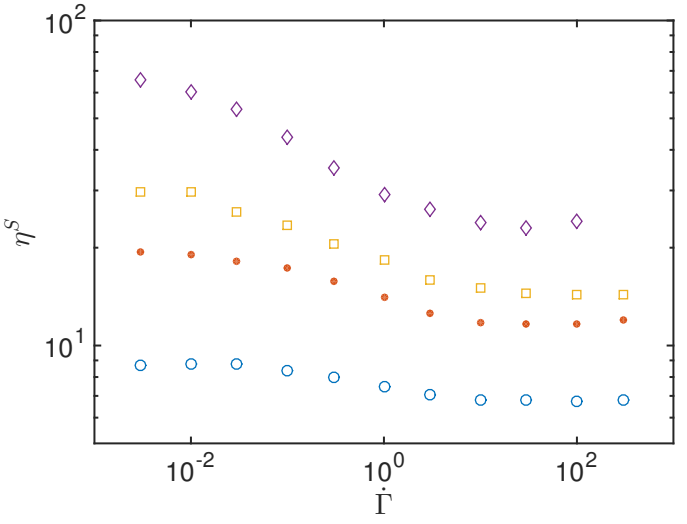

FIGURE 4. Relative viscosity as a function of the reduced shear rate. (○) $\phi = 40\%$ (●) $\phi = 45\%$ □ $\phi = 47\%$ ⋄ $\phi = 50\%$

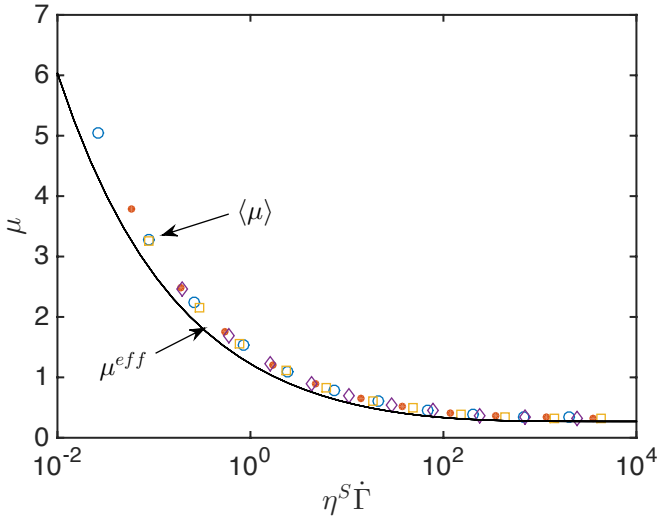

FIGURE 5. (●) Friction coefficient averaged over all contacting particle pairs. (○) $\phi = 40\%$ (●) $\phi = 45\%$ □ $\phi = 47\%$ ⋄ $\phi = 50\%$. Solid line : Effective friction coefficient from equation 3.4

the case for the lowest volume fraction ϕ=40%, and as the volume fraction increases, the curves shift toward lower reduced shear rate. This is expected, since the viscosity and more generally the stress level increase as ϕ increases, yielding a stronger contact force between particles at the same value of $\dot{\Gamma}$.

To get a deeper insight on this transition from high to low viscosity, the mean friction coefficient, $\langle\mu\rangle$, over all contacting particle pairs is displayed in figure 5 as a function of the reduced shear stress, $\eta^S\dot{\Gamma}$, which quantifies the force experienced by two contacting particles. A striking feature is that the data collapse on a single curve whatever the

ϕ_m^0	ϕ_m^∞	X^p	α_m^0	α_m^∞	X^a
0.700	0.546	2.43	1.00	0.640	1.85

TABLE 3. Fitting parameters of equation 3.2

particle volume fraction. This suggests that the reduced shear stress can be understood as the reduced effective normal force between contacting particles that controls the mean friction coefficient. The model built in section 3.3 is based on this idea.

3.2. *Constant friction coefficient*

Quite recent numerical studies concerning frictional non-Brownian suspensions demonstrated a strong influence of the friction coefficient μ, taken as a constant, on the effective viscosity (Mari *et al.* 2014; Gallier *et al.* 2014; Peters *et al.* 2016; Singh *et al.* 2018; Gallier *et al.* 2018). The key feature here is that the jamming volume fraction significantly depends on the friction coefficient. For instance, Mari *et al.* (2014), in their study of concentrated discontinuous shear-thickening suspensions, computed the high shear rate jamming volume fraction ϕ_m for three values of the microscopic friction coefficient, namely $\mu = 0$, $\mu = 1$ and $\mu = \infty$. The jamming volume fraction was shown to decrease from 0.66 to 0.56. More recently, Peters *et al.* (2016) and Singh *et al.* (2018) explained the variation of the viscosity of non-colloidal suspensions with the microscopic particle friction coefficient by a smooth decrease of the jamming volume fraction for microscopic friction coefficient ranging from 0 to 1. We note that such a correlation between jamming volume fraction and microscopic friction coefficient was evidenced in simulations of granular flows (Silbert 2010) and in experiments concerning discontinuous shear-thickening suspensions (Fernandez *et al.* 2013; Chatté *et al.* 2018).

We show here similar simulations where the friction coefficient is kept constant (table 2). For each value of μ, the following simple correlation law is fitted to the variation of the relative viscosity against the volume fraction :

$$\eta^S(\mu,\phi) = \frac{\alpha_0(\mu)}{\left(1-\frac{\phi}{\phi_m(\mu)}\right)^2} \tag{3.1}$$

The data from the simulation together with the respective correlation laws are displayed in figure 6 for two values of the friction coefficient. The fitting parameters are displayed in figure 7 against the friction coefficient μ, together with the best fit to equations 3.2, where the ϕ_m^x, α_0^x and X^x are again fitting parameters, that are gathered in table 3.

$$\begin{aligned}\phi_m &= \phi_m^\infty + (\phi_m^0 - \phi_m^\infty)\ \tfrac{exp(-X^p\ \mathrm{atan}(\mu)) - exp(-\pi X^p/2)}{1-exp(-\pi X^p/2)} \\ \alpha_m &= \alpha_m^\infty + (\alpha_m^0 - \alpha_m^\infty)\ \tfrac{exp(-X^a\ \mathrm{atan}(\mu)) - exp(-\pi X^a/2)}{1-exp(-\pi X^a/2)}\end{aligned} \tag{3.2}$$

In particular, the jamming volume fraction seems to approach the limit $\phi_m^\infty = 0.546$ as the friction coefficient goes to ∞ and is equal to $\phi_m^0 = 0.700$ for μ=0. These values are somewhat different from the values that can be found in litterature and that have been obtained from simulations performed at higher volume fraction. It is especially true for frictionless particles where the jamming fraction was estimated around 0.64 for $\mu = 0$ Mari *et al.* (2014); Gallier *et al.* (2018); Singh *et al.* (2018). This is not really a problem in the present article, since the same volume fraction range is kept throughout the study. In addition, our data are in quite good agreement with measurements performed with discontinuous shear-thickening suspensions in frictional regime (Fernandez *et al.* 2013).

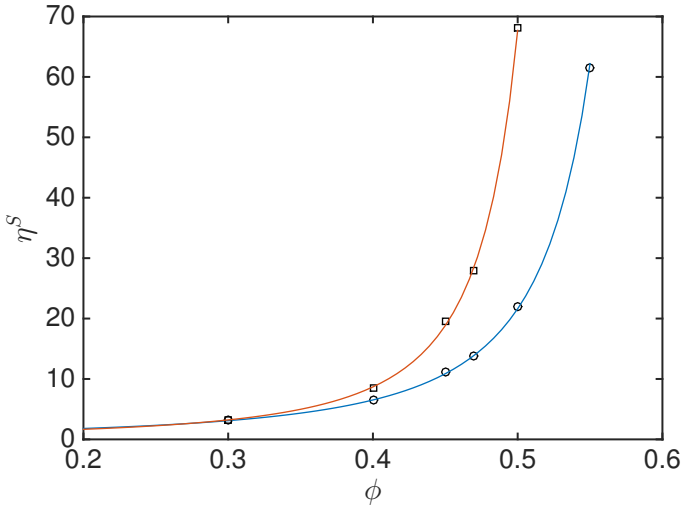

FIGURE 6. Shear viscosity against volume fraction for two values of the friction coefficient. (∘) $\mu = 0.27$ (□) $\mu = 2$. Solid line : best fit of equation 3.1 to the data.

The second fitting parameter, α_0 deserves a comment. Obviously, the correlation 3.1 is not suitable at low volume fraction, for which the value $\alpha_0 = 1$ is expected. In addition, its variation with the volume fraction is correlated to the variation of ϕ_m. It can be easily understood, noting that the viscosity from the simulations for any volume fraction lower than 0.3 hardly depends on the friction coefficient, so that the variation of ϕ_m has to be balanced in this volume fraction range. Finally, even though α_0 significantly decreases with the friction coefficient, the viscosity variations for sufficiently high volume fraction are mostly due to the variation of ϕ_m.

3.3. *Viscosity model*

In this section, we show that a simple model based on the correlation laws from the simulations with constant friction coefficient described in the previous section allows to precisely reproduce the viscosity that is simulated when the load-dependent friction is taken into account. Returning to the particles with load-dependent friction coefficient, we make the assumption that the viscosity can be computed from equations 3.1 and 3.2, provided that the relevant effective friction coefficient, μ^{eff}, is controlled by the reduced shear stress as proposed in section 3.1 and supported by the collapse of the mean friction coefficient with $\eta^S\dot{\Gamma}$ (see figure 5). We note that this approach is quite similar to that recently followed by Chatté *et al.* (2018) to explain their experimental results. Therefore, we obtain the following self-consistent expression for the shear-thinning suspension viscosity:

$$\eta^S(\dot{\Gamma},\phi) = \frac{\alpha_0(\mu^{eff}(\eta^S\dot{\Gamma}))}{\left(1-\frac{\phi}{\phi_m(\mu^{eff}(\eta^S\dot{\Gamma}))}\right)^2} \tag{3.3}$$

A very good prediction of the viscosity-shear stress behavior is obtained if the following

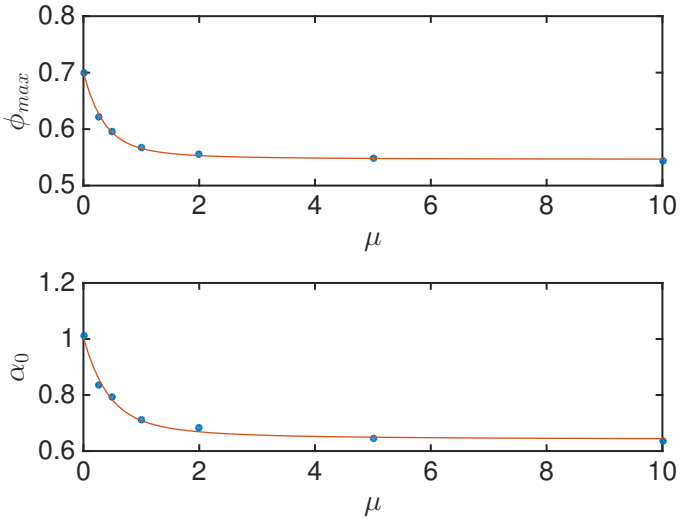

FIGURE 7. Fitting parameters of equation 3.1 as a function of the friction coefficient. • Simulation data. Solid line : best fit (equation 3.2)

expression of the effective friction coefficient is introduced in equation 3.3:

$$\mu^{eff} = 0.27 coth \left[0.27 \left(\frac{\eta^S \dot{\Gamma}}{1.69} \right)^{0.35} \right] \tag{3.4}$$

where the scaling factor 1.69 has been tuned in order the model to fit to the simulation data. The computed viscosity from equations 3.2, 3.3 and 3.4 is displayed in figure 8, in close agreement with the data from the simulation. It follows from this phenomenological model that the characteristic reduced force that controls friction, and consequently the viscosity, is proportional to the reduced shear stress:

$$\frac{\bar{F}_n}{L_c} = \frac{6\pi\eta_0\eta^S a_1^2 \dot{\gamma}}{1.69\ L_c} = \frac{\eta^S \dot{\Gamma}}{1.69} \tag{3.5}$$

It should be noted (figure 5), that the effective friction coefficient, μ^{eff}, which has been tuned in order the modeled viscosity to fit the simulated viscosity - shear stress behavior, is quite close to the mean friction coefficient, $\langle\mu\rangle$ that is a direct output of the simulations (Section 3.1).

Using equations 3.2 and 3.4, we can compute the variation of α_0 (solid line in figure 9) and ϕ_m (solid line in figure 10) with $\eta_S \dot{\Gamma}$. At low shear stress, where the friction coefficient diverges, the jamming volume fraction approaches the asymptotic value $\phi_m^\infty = 0.546$ for high friction coefficient (equation 3.2 and text thereafter). At high shear stress, ϕ_m levels off at the value 0.625 computed from equation 3.2 for the lowest friction coefficient 0.27 corresponding to infinite shear stress (equation 3.4).

To conclude this numerical section, it should be noted that the very good agreement between the data from the load-dependent friction simulations and the viscosity from equation 3.3 allows to check the influence of any particular friction law on the viscosity without need to perform new simulations. We follow this idea at the end of the experimental section.

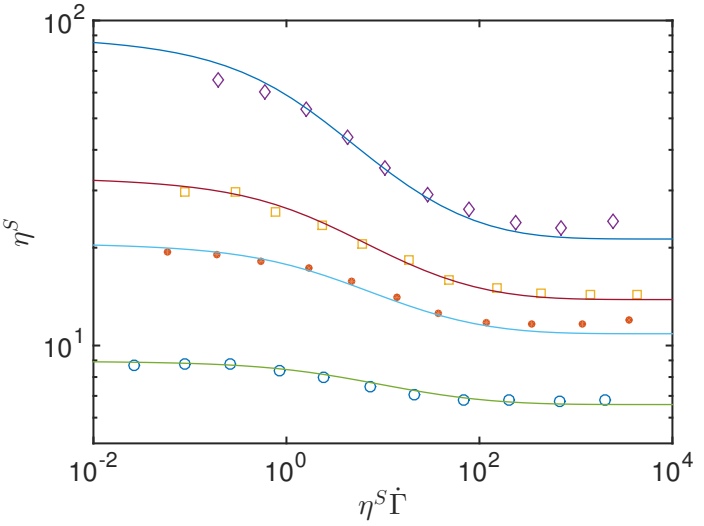

FIGURE 8. Viscosity as a function of reduced shear stress. Symbol : same data as in figure 4. Solid line : equation 3.3

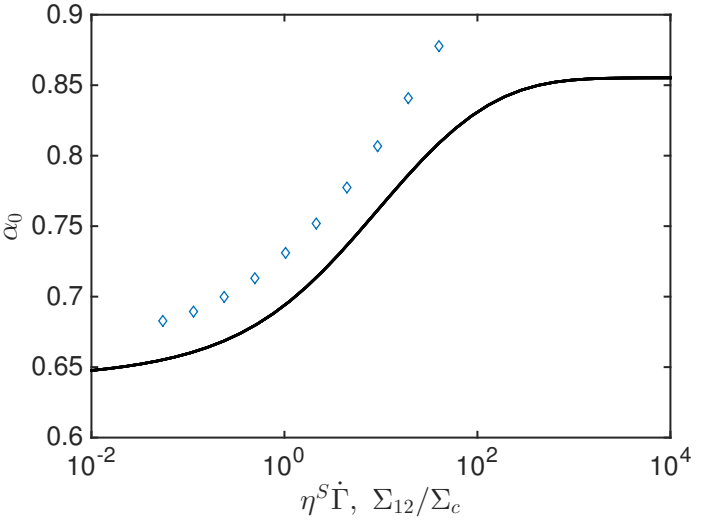

FIGURE 9. Second fitting parameter in the viscosity correlation (equation 3.1). Solid line : computed from equations 3.2 and 3.4. (◇) Experiments.

4. Experiments

4.1. *Suspensions*

The suspensions are made of polystyrene (PS) particles *(Dynoseed TS40, Microbeads)*, dispersed in silicon oil *(M 500, Roth)*. The particles are 40 μm in diameter with a relative standard deviation lower than 5 % and their roughness has been measured with Atomic Force Microscopy (see figure 11) and has been found to be around 36 nm which agrees closely with the results of Moon *et al.* (2015) who measured 32 nm and is not so far from the estimation of Garland *et al.* (2013) who measured a characteristic roughness height

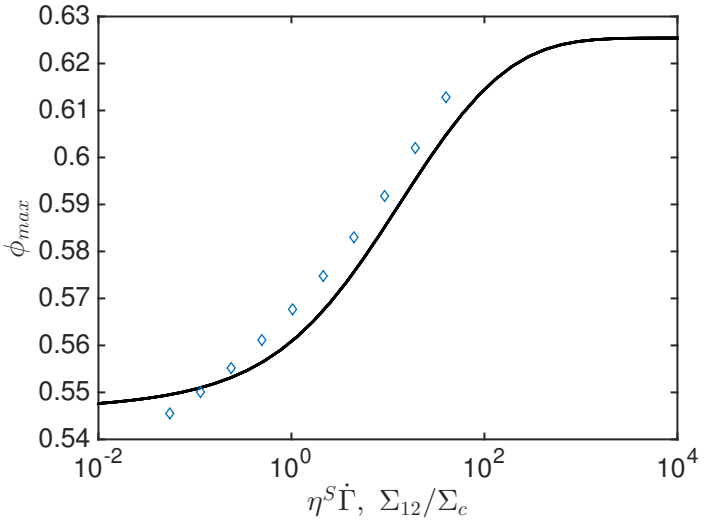

FIGURE 10. Jamming volume fraction as a function of reduced shear stress. Solid line : computed from equations 3.2 and 3.4. (⋄) Experiments.

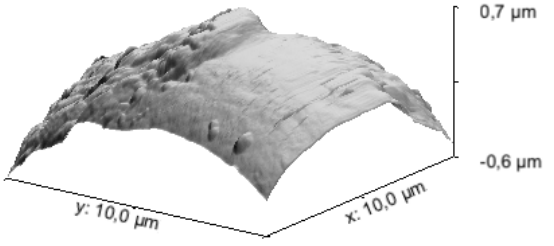

FIGURE 11. AFM image of a polystyrene particle.

around $100\,nm$. Before adding the particles to the suspending liquid, they are carefully washed with clear water and dried under vacuum at $60°C$ for 12 hours.

The particle density has been measured to be $1.044\ \pm 0.005\,g/cm^3$ and the density of the silicon oil to $0.972\,g/cm^3$ at $T = 25°C$. The viscosity of the suspending liquid, η_0, has been measured in cone-plate geometry. At $T = 25°C$, η_0 is measured to be $0.487\,Pa.s$ and shows no variation with shear rate in the tested range $5.10^{-1}s^{-1} < \dot{\gamma} < 250\,s^{-1}$. Five particle volume fractions have been tested : 0.4, 0.43, 0.45, 0.47 and 0.49, all at $T = 25°C$. Due to density mismatch between particles and silicon oil, it is necessary to measure the viscosity for stresses that are high enough for particles to be resuspended. The settling of the particles is controlled by the Shields parameter, Sh, that is the ratio of fluid force on the particle to the weight of the particle.

$$Sh = \frac{\tau}{2a\,\Delta\rho\,g} >> 1 \tag{4.1}$$

$Sh = 1$ for $\tau = 0.03\,Pa$ and in the experiments only stresses larger than $0.1\,Pa$ are applied so that particle settling is not expected to take place.

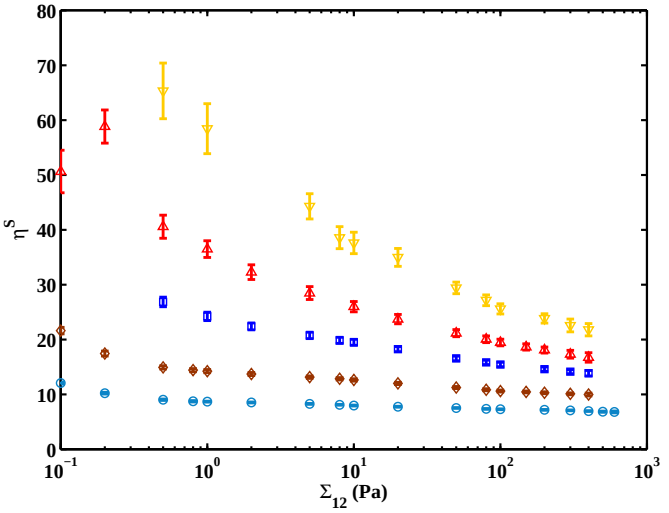

FIGURE 12. relative viscosity as a function of shear stress. Symbol : $40\mu m$ PS particles ($\circ$) $\phi = 0.4$. ($\diamond$) $\phi = 0.43$. ($\square$) $\phi = 0.45$ ($\triangle$) $\phi = 0.47$ ($\triangledown$) $\phi = 0.49$

4.2. *Rheometric measurements*

The viscosity has been measured in rotating parallel plate geometry. The radius of the disks, R, is $30\,mm$ and the gap height is set to $1\,mm$, i.e. 25 particle diameters. Rotating plate geometry provides the advantage that no migration (Chow *et al.* 1994) or very slow migration (Merhi *et al.* 2005) takes place. The drawback of using such a geometry to study non-Newtonian materials is obviously the variation of the shear rate magnitude over the gap. To account for shear rate variation from 0 at the center to $\dot{\gamma}_R = \Omega R/h$ at the rim, the Mooney-Rabinovitch correction is used :

$$\eta(\dot{\gamma}_R) = \eta_{mes}\left(1 + \frac{1}{4}\frac{d\,\ln(\eta_{mes})}{d\,\ln(\dot{\gamma}_R)}\right) \tag{4.2}$$

where $\eta_{mes} = \sigma_R/\dot{\gamma}_R$ is the apparent viscosity delivered by the rheometer, with σ_R the stress at the rim ($r = R$).

The shear stress ranges from 0.1 to $600\,Pa$ and each measurement is preceded by a preshear of $100\,Pa$ for a period of $20\,s$.

4.3. *Experimental results*

Figure 12 displays the shear rate dependence of the relative viscosity, $\eta_S = \eta/\eta_0$, corrected using the Mooney-Rabinovitch correction (Eq. 4.2) for the five particle volume fractions: 0.4, 0.43, 0.45, 0.47 and 0.49. The measurement uncertainties have been estimated by reloading five times the suspensions in the rheometer.

The shear-thinning behavior extends over a range of more than the three decades that have been tested and is more pronounced as the particle volume fraction increases. These results are very consistent with those of (Tanner & Dai 2016) obtained with the same particles (*Microbeads, TS40*) dispersed in a silicon oil (viscosity $1.1\,Pa.s.$) in a slightly narrower range of shear stress.

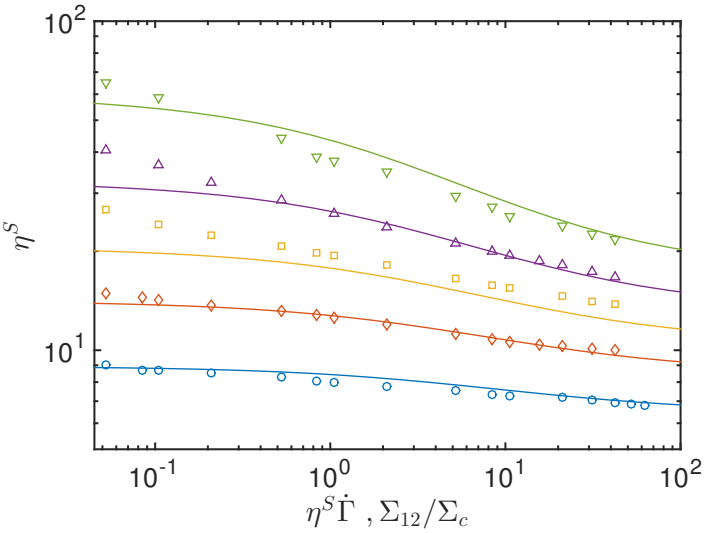

FIGURE 13. Viscosity as a function of reduced shear stress. $\phi = 0.4$, $\phi = 0.43$, $\phi = 0.45$, $\phi = 0.47$, $\phi = 0.49$. Symbol : experiments. Solid line : model (equation 3.3).

5. Discussion: comparison between experiments and simulations

No simulations were performed for $\phi = 0.43$ and $\phi = 0.49$. Since the model defined in equation 3.3 fits the simulation well, the experimental data are compared to the model. In addition, in order to draw the experimental and numerical data on the same figure, the critical stress Σ_c has to be stated so that $\eta^S\dot{\Gamma} = \Sigma_{12}/\Sigma_c$. We determine the value that fits the best: $\Sigma_c = 9.53\ Pa$. Figure 13 displays the suspension viscosity as a function of reduced shear stress, both experiments and model.

The experimental data are in quite good qualitative agreement with the model. The viscosity range for a given volume fraction is roughly the same in both cases, and is spanned over the same reduced stress range too. From the value of the fitted critical stress Σ_c=9.53 Pa , we can deduce the value of the critical load L_c: $L_c = \Sigma_c \times (6\pi a_1^2) = 46$ nN. As for the radius a_1, that is 0.8 times the mean radius of the bidisperse suspension in the simulations, we take $a_1 = 16\ \mu$m. The value of L_c yields an estimation of the asperity radius of curvature R^{exp}—h_r in the model—using equation 2.4 together with the material constant in table 1 : $R_{exp} \approx 156$ nm. We recall here that in the model, the asperity was considered as half a sphere of radius h_r. However, the typical extension of an asperity in the direction parallel to the surface $L_\parallel$ may be different from the asperity height $h_r \sim 36\,nm$. This extension may be estimated from the curvature: $L_\parallel \sim \sqrt{2R_{exp}h_r} \approx 3.4\,\mu m$. We did not perform extensive study of the surface roughness statistics. However, this value for the extension of an asperity is quite consistent with the AFM image displayed in figure 11. We note also that contact may occur through a few contact points instead of a single point as assumed in the model. The consequence would be qualitatively the same as increasing the radius of curvature, i.e. to increase the critical load. On the whole, this qualitative agreement suggests that the physical mechanism of the shear-thinning behavior is satisfactorily captured by the load-dependent friction model.

In more detail, the viscosity from the model (or the simulations) presents some discrepancies with the experimental values. At low shear stress, the experimental viscosity does not really show any plateau, contrarily to what is expected from the model or the

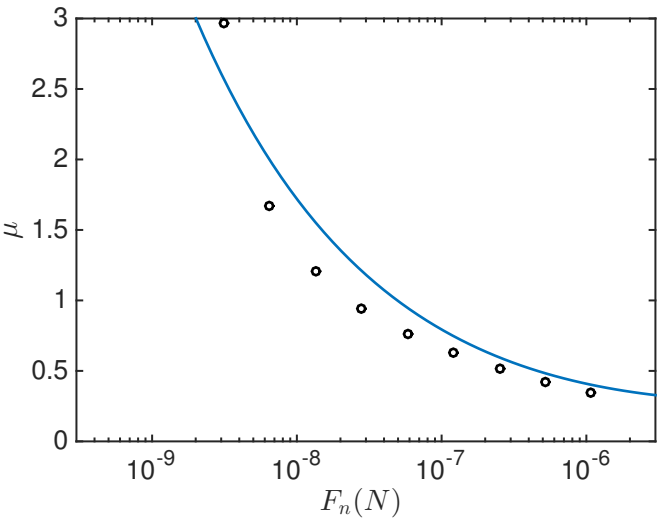

FIGURE 14. Microscopic friction coefficient. Symbol : experimental data. Solid line : mono-asperity model from equation 3.4 with $L_c = 46$ nN.

simulations. This difference may be explained by residual adhesion between particles regardless the great care that has been taken in the choice and in the preparation of the suspensions. Such adhesive interactions, even very small, should influence the viscosity at small enough shear stress. In the high stress range, the experimental measurement could not be performed at such high stresses that the viscosity plateau would be reached, due to the usual edge fracture in the parallel plate geometry.

To go further in the comparison between the model and the experiments, it is possible to compute for each stress the parameters of the viscosity model $\alpha_0(\Sigma_{12})$ and $\phi_m(\Sigma_{12})$ from the experimental data. These experimental parameters are displayed in figures 9 and 10, respectively, against the reduced shear stress, together with their numerical counterpart. We chose the same value of the critical stress $\Sigma_c = 9.53$ Pa as in figure 13. The variations of ϕ_m from the experiments and from the model are in quite good agreement, with approximately the same volume fraction range, and the same reduced stress range. However, the experimental jamming fraction takes one value under ϕ_m^∞ at low shear stress, possibly due to residual adhesion mentioned above. The experimental and numerical data for α_0 are in quite good agreement too, even though the experimental values are above the model. It should be stressed here that the values of α_0 and ϕ_m from the experiment significantly depend on the precise adjustment procedure, apparently due to the dispersion of the experimental data, especially in the low stress range, where the discrepancies are larger. It does not affect the qualitative shape of the ϕ_m curve, but leads to variations of $\Delta\phi_m \sim 0.01$.

Finally the effective friction coefficient $\mu^{eff}(\Sigma_{12})$ can be computed from the experimental jamming volume fraction (figure 10) reversing equation 3.2. We note that it is possible only for the values of the experimental jamming fraction included in the range of variation of ϕ_m found in the simulations with constant friction coefficient. It is then assumed, as previously in equation 3.4, that μ^{eff} is actually the microscopic friction coefficient for the applied load $\bar{F}_n = 6\pi a_1^2 \Sigma_{12}$ /1.69. The resulting experimental load-dependent friction coefficient is displayed in figure 14, together with the mono-asperity contact model. As expected, the experimental data are in quite satisfactory agreement

with the mono-asperity contact model, except for values of the force corresponding to values of ϕ_m smaller or close to the minimum value ϕ_m^∞ in the model, i.e. $F_n < 6$ nN.

6. Conclusion

In this paper it is shown that it is possible to capture the shear-thinning behavior observed in most non-Brownian frictional suspensions by considering variable friction interactions between particles. In the contact model that is considered in the present article, load-dependent friction coefficient is an attribute of mono-asperity elastic-plastic contact. And, owing to the low interparticle forces involved in sheared suspensions, it is expected that particles come into contact through one or a few asperities. To test this idea, we introduce in a numerical simulation code based on the Force Coupling Method a contact law adapted from the numerical work of Brizmer *et al.* (2007). The results of the simulations show a decrease of the viscosity with the shear stress that is in the same range as that observed experimentally. The comparison between simulations conducted either with constant friction coefficient or load-dependent friction coefficient made it possible to propose a model for the shear-thinning viscosity. As already shown by Peters *et al.* (2016) and Singh *et al.* (2018), the viscosity in the former case increases with the friction coefficient, mainly due to the decrease of the jamming volume fraction. In the proposed model for the particles with load-dependent friction coefficient, the effective friction coefficient μ^{eff} is specified by the effective normal contact force which is simply proportional to the shear stress. As the shear stress increases, μ^{eff} decreases and the jamming volume fraction increases, leading to the reduction of the viscosity. A very good agreement between the model and the simulations is found. These results are compared to experimental measurements carried out on suspensions of polystyrene particles (40 μm in diameter) dispersed in silicone oil for five particle volume fractions between 0.40 an 0.49. The overall agreement between the model (or the simulations) and the experiments is satisfactory. The viscosity reduction as the shear stress increases is well captured by the model and the variation of the jamming volume fraction with the shear stress is in quite good agreement with the predictions. The closeness between the experiments and the results of the model enabled us to evaluate the friction coefficient and its variation with the applied shear stress from rheometric measurements. Nevertheless, due to the complexity of contact at microscopic scale, and to the number of parameters that are potentially relevant in the surface physical chemistry, the next step to get a more quantitative understanding of the physical mechanism leading to this shear-thinning behavior would be to determine the friction law between particles from colloidal probe AFM measurements.

Acknowledgements

The authors thank Cyril Claudet and Olga Volkova for the AFM roughness measurements. This work was granted access to the HPC and visualization resources of "Centre de Calcul Interactif" hosted by "Université Nice Sophia Antipolis".

REFERENCES

Acrivos, Andreas, Fan, Xiaoxing & Mauri, Roberto 1994 On the measurement of the relative viscosity of suspensions. *Journal of Rheology* **38** (5), 1285–1296.

Archard, JF 1957 Elastic deformation and the laws of friction. *Proceedings of the Royal Society of London A: Mathematical, Physical and Engineering Sciences* **243** (1233), 190–205.

Benabdallah, SMH & Yelle, H 1991 Static and quasi-dynamic coefficient of friction of three

engineering thermoplastics: UHMWPE, PA 66, POM. *Journal of Materials Science* **26** (9), 2445–2450.

Biggs, Simon & Spinks, Geoffrey 1998 Atomic force microscopy investigation of the adhesion between a single polymer sphere and a flat surface. *Journal of adhesion science and technology* **12** (5), 461–478.

Blanc, Frédéric, Peters, François & Lemaire, Elisabeth 2011 Experimental signature of the pair trajectories of rough spheres in the shear-induced microstructure in noncolloidal suspensions. *Physical review letters* **107** (20), 208302.

Brizmer, V, Kligerman, Y & Etsion, I 2006*a* The effect of contact conditions and material properties on the elasticity terminus of a spherical contact. *International Journal of Solids and Structures* **43** (18), 5736–5749.

Brizmer, Victor, Kligerman, Yuri & Etsion, Izhak 2007 Elastic–plastic spherical contact under combined normal and tangential loading in full stick. *Tribology Letters* **25** (1), 61–70.

Brizmer, Victor, Zait, Yuval, Kligerman, Yuri & Etsion, Izhak 2006*b* The effect of contact conditions and material properties on elastic-plastic spherical contact. *Journal of mechanics of materials and structures* **1** (5), 865–879.

Butt, Hans-Jürgen, Cappella, Brunero & Kappl, Michael 2005 Force measurements with the atomic force microscope: Technique, interpretation and applications. *Surface science reports* **59** (1), 1–152.

Chang, WR, Etsion, I & Bogy, D BASME 1987 An elastic-plastic model for the contact of rough surfaces. *Journal of tribology* **109** (2), 257–263.

Chatté, Guillaume, Comtet, Jean, Niguès, Antoine, Bocquet, Lydéric, Siria, Alessandro, Ducouret, Guylaine, Lequeux, François, Lenoir, Nicolas, Ovarlez, Guillaume & Colin, Annie 2018 Shear thinning in non-brownian suspensions. *Soft matter* **14**, 879–893.

Chow, Andrea W, Sinton, Steven W, Iwamiya, Joseph H & Stephens, Thomas S 1994 Shear-induced particle migration in couette and parallel-plate viscometers: NMR imaging and stress measurements. *Physics of Fluids* **6** (8), 2561–2576.

Cundall, Peter A & Strack, Otto DL 1979 A discrete numerical model for granular assemblies. *geotechnique* **29** (1), 47–65.

Dbouk, Talib 2011 Rheology of concentrated suspensions and shear-induced migration. PhD thesis, Université Nice Sophia Antipolis.

Derjaguin, Boris V, Muller, Vladimir M & Toporov, Yu P 1975 Effect of contact deformations on the adhesion of particles. *Journal of Colloid and interface science* **53** (2), 314–326.

Ducker, William A, Senden, Tim J & Pashley, Richard M 1992 Measurement of forces in liquids using a force microscope. *Langmuir* **8** (7), 1831–1836.

Ecke, Stefan & Butt, Hans-Jürgen 2001 Friction between individual microcontacts. *Journal of colloid and interface science* **244** (2), 432–435.

Fernandez, Nicolas, Cayer-Barrioz, Juliette, Isa, Lucio & Spencer, Nicholas D 2015 Direct, robust technique for the measurement of friction between microspheres. *Langmuir* **31** (32), 8809–8817.

Fernandez, Nicolas, Mani, Roman, Rinaldi, David, Kadau, Dirk, Mosquet, Martin, Lombois-Burger, Hélène, Cayer-Barrioz, Juliette, Herrmann, Hans J, Spencer, Nicholas D & Isa, Lucio 2013 Microscopic mechanism for shear thickening of non-brownian suspensions. *Physical review letters* **111** (10), 108301.

Gadala-Maria, F & Acrivos, Andreas 1980 Shear-induced structure in a concentrated suspension of solid spheres. *Journal of Rheology* **24** (6), 799–814.

Gallier, Stany, Lemaire, Elisabeth, Peters, François & Lobry, Laurent 2014 Rheology of sheared suspensions of rough frictional particles. *Journal of Fluid Mechanics* **757**, 514–549.

Gallier, Stany, Peters, François & Lobry, Laurent 2018 Simulations of sheared dense non-colloidal suspensions: evaluation of the role of long-range hydrodynamics. *To be published in Phys. Rev. Fluids* .

Garland, S, Gauthier, G, Martin, J & Morris, JF 2013 Normal stress measurements in sheared non-brownian suspensions. *Journal of Rheology* **57** (1), 71–88.

Greenwood, JA & Williamson, JBP 1966 Contact of nominally flat surfaces. *Proceedings of the Royal Society of London. Series A, Mathematical and Physical Sciences* **295** (1442), 300–319.

Heim, Lars O, Ecke, Stefan, Preuss, Markus & Butt, Hans-Jürgen 2002 Adhesion forces between individual gold and polystyrene particles. *Journal of adhesion science and technology* **16** (7), 829–843.

Johnson, KL, Kendall, K & Roberts, AD 1971 Surface energy and the contact of elastic solids. *Proceedings of the Royal Society of London A: Mathematical, Physical and Engineering Sciences* **324** (1558), 301–313.

Li, YQ, Tao, NJ, Pan, J, Garcia, AA & Lindsay, SM 1993 Direct measurement of interaction forces between colloidal particles using the scanning force microscope. *Langmuir* **9** (3), 637–641.

Ling, Xing, Butt, Hans-Jürgen & Kappl, Michael 2007 Quantitative measurement of friction between single microspheres by friction force microscopy. *Langmuir* **23** (16), 8392–8399.

Mari, Romain, Seto, Ryohei, Morris, Jeffrey F & Denn, Morton M 2014 Shear thickening, frictionless and frictional rheologies in non-brownian suspensions. *Journal of Rheology* **58** (6), 1693–1724.

McFarlane, JS & Tabor, D 1950 Relation between friction and adhesion. *Proceedings of the Royal Society of London. Series A, Mathematical and Physical Sciences* pp. 244–253.

Merhi, Dima, Lemaire, Elisabeth, Bossis, Georges & Moukalled, Fadl 2005 Particle migration in a concentrated suspension flowing between rotating parallel plates: Investigation of diffusion flux coefficients. *Journal of Rheology* **49** (6), 1429–1448.

Moon, Ji Young, Dai, Shaocong, Chang, Li, Lee, Joon Sang & Tanner, Roger I 2015 The effect of sphere roughness on the rheology of concentrated suspensions. *Journal of Non-Newtonian Fluid Mechanics* **223**, 233–239.

Myshkin, NK, Petrokovets, MI & Kovalev, AV 2006 Tribology of polymers: adhesion, friction, wear, and mass-transfer. *Tribology International* **38** (11), 910–921.

Ness, Christopher & Sun, Jin 2015 Flow regime transitions in dense non-brownian suspensions: Rheology, microstructural characterization, and constitutive modeling. *Physical Review E* **91** (1), 012201.

Ovcharenko, A, Halperin, G & Etsion, I 2008 Experimental study of adhesive static friction in a spherical elastic-plastic contact. *Journal of Tribology* **130** (2), 021401.

Pednekar, Sidhant, Chun, Jaehun & Morris, Jeffrey F 2018 Bidisperse and polydisperse suspension rheology at large solid fraction. *Journal of Rheology* **62** (2), 513–526.

Peters, François, Ghigliotti, Giovanni, Gallier, Stany, Blanc, Frédéric, Lemaire, Elisabeth & Lobry, Laurent 2016 Rheology of non-brownian suspensions of rough frictional particles under shear reversal: A numerical study. *Journal of rheology* **60** (4), 715–732.

Pham, Phong, Metzger, Bloen & Butler, Jason E 2015 Particle dispersion in sheared suspensions: Crucial role of solid-solid contacts. *Physics of Fluids* **27** (5), 051701.

Reitsma, Mark, Craig, Vince & Biggs, Simon 2000 Elasto-plastic and visco-elastic deformations of a polymer sphere measured using colloid probe and scanning electron microscopy. *International journal of adhesion and adhesives* **20** (6), 445–448.

Schaefer, DM, Carpenter, M, Gady, B, Reifenberger, R, Demejo, LP & Rimai, DS 1995 Surface roughness and its influence on particle adhesion using atomic force techniques. *Journal of adhesion science and technology* **9** (8), 1049–1062.

Seto, Ryohei, Giusteri, Giulio G. & Martiniello, Antonio 2017 Microstructure and thickening of dense suspensions under extensional and shear flows. *Journal of Fluid Mechanics* **825**, R3.

Seto, Ryohei, Mari, Romain, Morris, Jeffrey F & Denn, Morton M 2013 Discontinuous shear thickening of frictional hard-sphere suspensions. *Physical review letters* **111** (21), 218301.

Shäfer, J, Dippel, S & Wolf, D 1996 Force schemes in simulations of granular materials. *J. Phys. I France* **6**, 5–20.

Silbert, Leonardo E 2010 Jamming of frictional spheres and random loose packing. *Soft Matter* **6** (13), 2918–2924.

Singh, Abhinendra, Mari, Romain, Denn, Morton M & Morris, Jeffrey F 2018 A constitutive model for simple shear of dense frictional suspensions. *Journal of Rheology* **62** (2), 457–468.

Tabor, David 1981 Friction—the present state of our understanding. *J. Lubr. Technol* **103** (2), 169–179.

Tanner, Roger I & Dai, Shaocong 2016 Particle roughness and rheology in noncolloidal suspensions. *Journal of Rheology* **60** (4), 809–818.

Vazquez-Quesada, Adolfo, Mahmud, Arif, Dai, Shaocong, Ellero, Marco & Tanner, Roger I 2017 Investigating the causes of shear-thinning in non-colloidal suspensions: Experiments and simulations. *Journal of Non-Newtonian Fluid Mechanics* .

Vázquez-Quesada, Adolfo, Tanner, Roger I & Ellero, Marco 2016 Shear thinning of noncolloidal suspensions. *Physical review letters* **117** (10), 108001.

Yeo, Kyongmin & Maxey, Martin R 2010 Simulation of concentrated suspensions using the force-coupling method. *Journal of computational physics* **229** (6), 2401–2421.

Zarraga, Isidro E, Hill, Davide A & Leighton Jr, David T 2000 The characterization of the total stress of concentrated suspensions of noncolloidal spheres in newtonian fluids. *Journal of Rheology* **44** (2), 185–220.

Zou, Yi, Jayasuriya, Sunil, Manke, Charles W & Mao, Guangzhao 2015 Influence of nanoscale surface roughness on colloidal force measurements. *Langmuir* **31** (38), 10341–10350.